

# Efficient high-order accurate Fresnel diffraction via areal quadrature and the nonuniform FFT

Alex H. Barnett<sup>a,\*</sup>

<sup>a</sup>Center for Computational Mathematics, Flatiron Institute, Simons Foundation, New York, NY, USA, 10010

**Abstract.** We present a fast algorithm for computing the diffracted field from arbitrary binary (hard-edged) planar apertures and occulters in the scalar Fresnel approximation, for up to moderately high Fresnel numbers ( $\lesssim 10^3$ ). It uses a high-order *areal quadrature* over the aperture, then exploits a single 2D *nonuniform* fast Fourier transform (NUFFT) to evaluate rapidly at target points (of order  $10^7$  such points per second, independent of aperture complexity). It thus combines the high accuracy of edge integral methods with the high speed of Fourier methods. Its cost is  $\mathcal{O}(n^2 \log n)$ , where  $n$  is the linear resolution required in source and target planes, to be compared with  $\mathcal{O}(n^3)$  for edge integral methods. In tests with several aperture shapes, this translates to between 2 and 5 orders of magnitude acceleration. In starshade modeling for exoplanet astronomy, we find that it is roughly  $10^4 \times$  faster than the state of the art in accurately computing the set of telescope pupil wavefronts. We provide a documented, tested MATLAB/Octave implementation.

An appendix shows the mathematical equivalence of the boundary diffraction wave, angular integration, and line integral formulae, then analyzes a new *non-singular* reformulation that eliminates their common difficulties near the geometric shadow edge. This supplies a robust edge integral reference against which to validate the main proposal.

**Keywords:** Fresnel, diffraction, quadrature, numerical, nonuniform FFT, starshade.

\* [abarnett@flatironinstitute.org](mailto:abarnett@flatironinstitute.org)

## 1 Introduction

The numerical modeling of wave diffraction from thin two-dimensional (2D) screens and apertures in the Fresnel regime has many applications in optics<sup>1</sup> and acoustics [2, §8.4], including instrument modeling,<sup>3,4</sup> lithography mask design,<sup>5</sup> Fourier optics,<sup>6</sup> coherent X-rays,<sup>7</sup> acoustic emission,<sup>8</sup> computer-generated binary holograms,<sup>9</sup> starshades,<sup>10</sup> and Fresnel zone plate imagers.<sup>11,12</sup> This usually involves a plane or spherical wavefront hitting a binary (“0-1”) mask of given shape, although continuous opacity/phase variation is also possible. We will confine ourselves to the former case, although the method can trivially accommodate the latter. Our point is to present a simple—yet seemingly overlooked—method which renders their high-accuracy numerical modeling at moderate Fresnel numbers orders of magnitude more efficient than before.

One motivation is starshade design.<sup>10,13–17</sup> Given a space telescope, the goal is that a distant binary occulter blocks the direct light from a star, allowing much dimmer exoplanets separated from it by only tens of milli-arcseconds to be imaged. The occulter shape and distance are thus optimized to give a deep shadow region, with relative intensity of order  $10^{-10}$  across the telescope pupil, throughout a given wavelength range, while minimizing the occulter’s physical size (for practical reasons), and angular size at the telescope. This has led to shapes with “petals” that emulate a continuous radial apodization, radii of order 10 m, and distances of order  $10^7$  m. Here the scalar<sup>18</sup> and Fresnel approximations are superb [17, App. A], with a small Fresnel number (defined below) of typically 5–20. Numerical modeling is challenging, demanding at least 6-digit accuracy in amplitude to validate the shadow, and many runs with different wavelengths and shapes to assess mechanical and thermal stability.<sup>16</sup>

Fixing a wavelength  $\lambda$  and propagation distance  $z$ , a point in the aperture (or occulter) plane is  $(x, y, 0)$ , while a target point in the detector (or pupil) plane is  $(\xi, \eta, z)$ ; see Fig. 1. We drop the

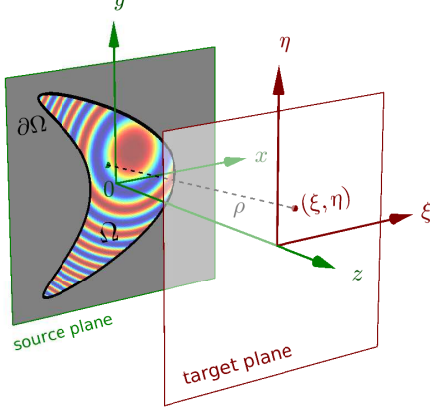


**Fig 1** Geometry and notation for Fresnel diffraction, in the case of  $\Omega$  an aperture with boundary  $\partial\Omega$ . A plane wave is incident from behind, along the  $z$  axis. For the target  $(\xi, \eta)$ , the real part of the integrand in (1) is imaged in color (red positive, blue negative, and green around zero; each red or blue annular region is a *Fresnel zone*).

constant  $z$ -coordinates from now on: the problem is in essence 2D. In the case of a unit amplitude plane wave with wavevector  $(0, 0, 2\pi/\lambda)$  incident on a planar aperture  $\Omega \subset \mathbb{R}^2$ , the mathematical task is to evaluate the Fresnel integral for the scalar potential

$$u^{\text{ap}}(\xi, \eta) = \frac{1}{i\lambda z} \iint_{\Omega} e^{\frac{i\pi}{\lambda z} [(\xi-x)^2 + (\eta-y)^2]} dx dy . \quad (1)$$

This takes the form of a 2D convolution of the aperture's characteristic function  $\chi_{\Omega}$  with a radially-symmetric kernel (complex Gaussian), whose half-wave oscillation regions are commonly called “zones” (Fig. 1). If  $R$  is an effective (or maximum) radius of  $\Omega$ , then the in-plane separation  $r := \sqrt{(\xi-x)^2 + (\eta-y)^2}$  is typically bounded by  $R$  times a small constant. Thus the number of zones inside  $\Omega$  is of order

$$f := \frac{R^2}{\lambda z} \quad (\text{Fresnel number}) , \quad (2)$$

and the finest oscillation scale of the integrand is  $\mathcal{O}(1/f)$ . In (1) the prefactor  $1/i\lambda z$  insures that  $u$  tends to unity in the limit of large aperture, ie, the unimpeded wave.

It is worth reviewing the origin of (1). It arises from the Kirchhoff diffraction approximation to the full Maxwell equations; this is good when aperture features are much larger than  $\lambda$  [6, Ch. 3]. Only the zeroth and first term in the Taylor expansion of the exponent in the free-space Green's function  $e^{2\pi i \rho/\lambda}/\rho$  are then kept,  $\rho = \sqrt{r^2 + z^2}$  being the source-target distance (dotted line in Fig. 1). The Fresnel approximation is thus valid to the extent that the next term is small, implying the condition  $r^4 \ll \lambda z^3$ . The denominator of the Green's function is approximated by  $z$ . We refer the reader to [1, §8.3.3] [6, Ch. 4] for details. Note that the zeroth term gave the plane propagation phase  $e^{2\pi i z/\lambda}$ , which is usually included as a prefactor in (1). We drop it for simplicity; it is trivial to insert. By replacing  $z^{-1}$  by  $z^{-1} + D^{-1}$ , (1) also applies when a source at distance  $D$  produces a spherical incident wave.<sup>1,17,19</sup> In the plane wave case, by Babinet's principle [1, §8.3.2] [14, §2.2], the potential when  $\Omega$  defines an occulter rather than an aperture is simply given by

$$u^{\text{oc}}(\xi, \eta) = 1 - u^{\text{ap}}(\xi, \eta) . \quad (3)$$

Analytical forms for the integral (1) are known only for the straight edge, infinite slit, and rectangles (all involving the same 1D special function) [1, §8.7] [6, §4.5.1], and even the disc

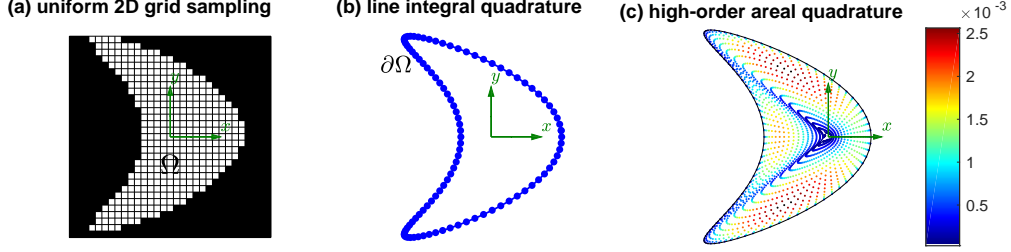


**Fig 2** Sketch of three alternative methods for discretization in the source (aperture) plane, shown for a kite-shaped aperture  $\Omega$  with smooth boundary  $\partial\Omega$ . (a) and (b) are established. Our method is (c): areal nodes  $(x_j, y_j)$  are shown with their color indicating the weights  $w_j$  according to the scale at the right.

gives analytical expressions only in the near-axis limit.<sup>20,21</sup> Semi-analytical Bessel expansions can be useful for symmetric starshade design.<sup>10,14</sup> But for general shapes one is left with fully numerical methods, which fall into two main categories (sketched in Fig. 2(a-b)):

- (a) 2D Fast Fourier transform (FFT) methods. There are two flavors: (i) methods implementing the convolution theorem (forward then backward FFTs), useful only for large  $f$  (near-field), or (ii) methods exploiting the quadratic form in (1) via a single FFT,<sup>11,13,22</sup> useful from zero to moderate  $f$ . See<sup>23</sup> for a review, where fractional FFTs are also considered. The FFT of course requires only  $\mathcal{O}(n^2 \log n)$  operations to transform a  $n \times n$  source to target grid. However, the aperture or occulter must be sampled (quantized) on the source grid, and if this is done in a binary fashion<sup>11</sup> (as in Fig. 2(a)), the error convergence rate is very low order, no faster than  $\mathcal{O}(1/n)$ . This is inadequate for starshade shadow modeling.<sup>14,15</sup> Sub-pixel averaging can improve accuracy,<sup>3,17</sup> but this can give at best<sup>24</sup>  $\mathcal{O}(1/n^2)$ , and for starshades huge ( $n > 10^5$ ) sized FFTs are still needed to reach the needed accuracy.<sup>17</sup> The underlying problem is that  $\chi_\Omega$  is *not a bandlimited function*, so is always poorly represented on regular grids.
- (b) Edge integral methods. Such methods discretize a target-dependent integral over the aperture/occluder boundary  $\partial\Omega$ . The literature splits into two formulae: (i) the “boundary diffraction wave” (BDW) of Miyamoto–Wolf,<sup>25</sup> arising from the Kirchhoff approximation, vs (ii) reduction of (1) to a 1D angular integral, due to Dager<sup>19</sup> and Dubra–Ferrari.<sup>21</sup> To resolve the Fresnel integrand, the number of discretization nodes must scale as  $n = \mathcal{O}(f)$ , so the cost for (direct) evaluation on a resolved  $n \times n$  target grid is  $\mathcal{O}(n^3) = \mathcal{O}(f^3)$ . Both formulae are applied to state of the art starshade modeling: Cady<sup>15,26</sup> uses (i), while Cash<sup>14</sup> and Harness et al.<sup>17</sup> use (ii). Here 2<sup>nd</sup>-order, ie  $\mathcal{O}(1/n^2)$  accurate, midpoint quadrature rules are used, with up to about  $10^5$  nodes, to reach the needed 6-digit accuracy.

**Remark 1.** *Such edge integral methods should not be confused with the (more involved) boundary integral equation (BIE) method, which solves the 3D Helmholtz or Maxwell equations using surface unknowns.*<sup>27,28</sup>

Our proposal combines the best features of the above two categories, namely the speed of the FFT methods with the high (and potentially high-order) accuracy of edge integral methods for binary apertures. The result is an acceleration over edge integral methods of between 2 and 5 orders of magnitude. In a nutshell the idea is, realizing that a 2D regular grid guarantees poor

quadrature for integrals over  $\Omega$ , to replace it with a much better (high-order) *areal quadrature scheme*; see Fig. 2(c). Then exploiting the quadratic form in (1), as in “single FFT” methods (a)(ii), leaves one remaining problem: how to rapidly evaluate Fourier sums involving off-grid frequencies. Fortunately, fast algorithms for this task—nonuniform FFTs<sup>29,30</sup>—are quite mature, and have speeds only one order of magnitude below those of plain FFTs.

High accuracy relies on constructing a good areal quadrature for  $\Omega$ , which depends on its geometric description. We show that such quadratures can easily piggyback off boundary quadratures, or be built independently. Our proposal is in some way related to diffraction methods that subsample the FFT<sup>31</sup> or use chirp FFTs;<sup>4</sup> however, it is much simpler and more general than either.

Turning to the structure of this paper, Sec. 2 explains the method for arbitrary targets (Sec. 2.1), then gridded targets (Sec. 2.2), the latter being somewhat faster. In Sec. 3 we demonstrate the high accuracy and efficiency of the method for a smooth occulter (Sec. 3.1), two symmetric starshades (Sec. 3.2), and an aperture built from 67 million triangles (Sec. 3.3). We compare to the performance of a BDW edge integral code.<sup>15,26</sup> We draw conclusions and propose extensions in Sec. 4.

Finally, validating the proposed NUFFT method down to errors of  $10^{-12}$  or better demanded a high-accuracy reference edge integral method, which required new research, to which the Appendix is devoted. There we clarify that *the BDW edge-integral (b)(i) and angular-integration (b)(ii) methods are equivalent*, and equivalent to a more convenient line integral due to Cash.<sup>14</sup> However, as we show, existing edge integral methods suffer numerical breakdown as targets approach  $\partial\Omega$  (the geometric shadow edge), because they represent the (smooth) diffracted field as a *sum of two discontinuous terms, one with a singular integrand*. We instead present and analyze a simple, robust *non-singular line integral* (NSLI) that maintains close to machine accuracy for target points near or even on  $\partial\Omega$ , without extra work, yet takes only five lines to code.

**Remark 2.** *We maintain a documented, tested, open-source MATLAB/Octave implementation of the proposed fast algorithm (using the FINUFFT library<sup>32</sup>), and the NSLI, on GitHub.<sup>33</sup> Queries to the author are welcome.*

## 2 The proposed method

Given a set of targets  $(\xi_k, \eta_k)$ ,  $k = 1, \dots, M$ , recall that the goal is to approximate (1) efficiently, ie, to evaluate

$$u_k^{\text{ap}} := u^{\text{ap}}(\xi_k, \eta_k) = \frac{1}{i\lambda z} \iint_{\Omega} e^{\frac{i\pi}{\lambda z} [(\xi_k - x)^2 + (\eta_k - y)^2]} dx dy, \quad k = 1, \dots, M. \quad (4)$$

Suppose that an *areal quadrature rule* for the aperture  $\Omega$  has been found, that is, a set of nodes  $(x_j, y_j) \in \mathbb{R}^2$  and weights  $w_j$ ,  $j = 1, \dots, N$ , such that, for all sufficiently smooth functions  $f$ ,

$$\iint_{\Omega} f(x, y) dx dy \approx \sum_{j=1}^N f(x_j, y_j) w_j \quad (5)$$

holds to high accuracy. Specifically, one seeks a family of rules of increasing  $N$ , with a high order of convergence,  $p$ , meaning that, for each  $C^\infty$ -smooth  $f$ , the error (difference between left and right hand sides) is  $\mathcal{O}(N^{-p})$ . This may even hold for all  $p > 0$ , in which case the convergence is said to be super-algebraic or *spectral*. For instance, such a quadrature over a rectangle is given by a tensor product of 1D Gauss–Legendre rules [34, Ch. 19]. By passing those nodes through a

smooth mapping of  $\mathbb{R}^2$  to  $\mathbb{R}^2$  (and multiplying the weights by its Jacobean), such rules for triangles and distorted quadrilaterals are easily made, the union of which can approximate any domain with piecewise smooth boundary to high order. For more node-efficient quadratures we refer the reader to recent works on triangles,<sup>35</sup> polygons,<sup>36,37</sup> and domains defined by piecewise rational curves.<sup>38</sup> Converting a *general* boundary into an areal quadrature for its interior is a software engineering task beyond the scope of this paper. We will be content constructing areal quadratures for three types of domains: the interior of a smooth closed curve, symmetric starshades, and unions of triangles.

Since any rule (5) must resolve the Fresnel integrand oscillations, for a fixed  $\Omega$  its number of nodes must grow like

$$N = \mathcal{O}(f^2). \quad (6)$$

Now simply applying (5) to (4) gives a high-order accurate direct (slow) summation method, that, as the results below show, can exceed accuracy requirements with reasonable numbers of nodes.<sup>1</sup> The cost of this direct sum to  $M$  targets would be  $\mathcal{O}(NM)$ ; our goal is now to reduce this to close to  $\mathcal{O}(N + M)$  via fast Fourier methods.

### 2.1 The fast algorithm for diffraction to arbitrary target points

We apply (5) to (4), then in the second line expand each quadratic term, to give

$$u_k^{\text{ap}} \approx \frac{1}{i\lambda z} \sum_{j=1}^N e^{\frac{i\pi}{\lambda z} [(\xi_k - x_j)^2 + (\eta_k - y_j)^2]} w_j \quad (7)$$

$$= \frac{1}{i\lambda z} e^{\frac{i\pi}{\lambda z} (\xi_k^2 + \eta_k^2)} \cdot \sum_{j=1}^N e^{\frac{-2\pi i}{\lambda z} (\xi_k x_j + \eta_k y_j)} \left( e^{\frac{i\pi}{\lambda z} (x_j^2 + y_j^2)} w_j \right). \quad (8)$$

This factorized form allows a three-step “fast” (in the sense of quasi-optimal scaling) algorithm:

1. Compute all “strengths”  $c_j$  according to the following, which takes  $\mathcal{O}(N)$  effort:

$$c_j := e^{\frac{i\pi}{\lambda z} (x_j^2 + y_j^2)} w_j, \quad j = 1, \dots, N.$$

2. Evaluate

$$v_k = \sum_{j=1}^N e^{\frac{-2\pi i}{\lambda z} (\xi_k x_j + \eta_k y_j)} c_j, \quad k = 1, \dots, M, \quad (9)$$

which is precisely the task performed by the so-called 2D nonuniform FFT (NUFFT) of type 3,<sup>29,30</sup> a well-established algorithm with modern software implementations.<sup>32,39</sup> This takes  $\mathcal{O}(N + M + q^2 \log q)$  effort, where  $q = \mathcal{O}(f)$  is the largest magnitude of the exponent in (9).

3. Post-multiply all outputs by their quadratic phases, which takes  $\mathcal{O}(M)$  effort:

$$u_k^{\text{ap}} = \frac{1}{i\lambda z} e^{\frac{i\pi}{\lambda z} (\xi_k^2 + \eta_k^2)} v_k, \quad k = 1, \dots, M.$$

The overall cost is thus  $\mathcal{O}(N + f^2 \log f + M)$ , Recalling (6), this is  $\mathcal{O}(f^2 \log f + M)$ . The NUFFT requires a user-chosen error tolerance  $\varepsilon$  which affects the prefactor of this run-time scaling, but rather weakly.<sup>32</sup>

---

<sup>1</sup>Our results show that claims such as “a single point in the shadow plane can require a trillion sine calculations at quadruple precision”<sup>14</sup> are overly pessimistic.

## 2.2 The fast algorithm for target points lying on a grid

Often sampling the diffracted wave on a dense regular Cartesian grid is sufficient. In this special case yet more speed can be gained. Specifically, let  $(\xi_k, \eta_k)$  be the 2D grid points defined by the product of  $n$ -point regular 1D grids

$$\{-nh/2, (-n/2 + 1)h, \dots, -h, 0, h, \dots, (n/2 - 1)h\}$$

in the  $\xi$  and  $\eta$  directions,  $h$  being the grid spacing. We assume  $n$  is even. This grid has  $M = n^2$  targets, and (ignoring its left-most column and bottom row) is centered on the origin. If we relabel the grid points as  $(hk_1, hk_2)$  for integer indices  $-n/2 \leq k_1, k_2 < n/2$ , and define rescaled source points  $\tilde{x}_j := (2\pi h/\lambda z)x_j$  and  $\tilde{y}_j := (2\pi h/\lambda z)y_j$ , the middle step (9) can be written

$$v_{k_1, k_2} = \sum_{j=1}^N e^{-i(k_1 \tilde{x}_j + k_2 \tilde{y}_j)} c_j, \quad -n/2 \leq k_1, k_2 < n/2,$$

which is precisely the so-called type 1<sup>29</sup> (or adjoint<sup>30</sup>) NUFFT. Its nonuniform points  $(\tilde{x}_j, \tilde{y}_j)$  are only defined modulo  $2\pi$ , and may need to be “folded” back into a valid input domain such as  $[-\pi, \pi)^2$ . If the grid width is similar in size to  $\Omega$ , then it is easy to check that such a folding is only needed if  $n$  is less than of order  $f$ , ie, the target grid under-resolves the diffracted field  $u$ . This is probably not a common use case.

The total cost for the regular grid case is  $\mathcal{O}(N + M \log M)$ , which, recalling (6) and  $n = \mathcal{O}(f)$ , is  $\mathcal{O}(f^2 \log f)$ . In practice, we find that for the same number  $M$  of targets spanning the same domain, and the same tolerance  $\varepsilon$ , this regular grid version is around four times faster than the above arbitrary target version, because the type 1 NUFFT is faster than the type 3 for the same space-bandwidth product.<sup>32</sup> The generalization to translated, rectangular target grids is simple, achieved through pre-phasing in step 1, and we will not present it here.

## 3 Performance tests and results

We now test the accuracy and speed of the above method in several geometries, and compare it to two edge integral methods. All codes are written in MATLAB R2017a, apart from FINUFFT which is a multithreaded C++ library with MEX interface. All timings will be reported for double-precision arithmetic on a 4-core i7-7700HQ laptop with 32GB RAM. In each case we will first need to describe the areal quadrature used.

### 3.1 Domains defined by a simple smooth closed curve

We will start by setting up a simple areal quadrature for the interior of a simple smooth closed curve. Suppose we have good quadrature nodes  $(X_i, Y_i) \in \partial\Omega$  and weights  $(W_i, V_i)$ , indexed by  $i = 1, \dots, n$ , for *vector* line integrals on  $\partial\Omega$ , that is, for all sufficiently smooth vector functions  $\mathbf{f}$  on  $\partial\Omega$ ,

$$\int_{\partial\Omega} \mathbf{f}(x, y) \cdot ds \approx \sum_{i=1}^n \mathbf{f}(X_i, Y_i) \cdot (W_i, V_i), \quad (10)$$

where  $ds$  is the counter-clockwise vector line element on  $\partial\Omega$ . Now fix a number of “radial” nodes  $m$ , and let  $\{\alpha_l\}_{l=1}^m$  be the Gauss–Legendre [34, Ch. 19] nodes, and  $\{\tilde{w}_l\}_{l=1}^m$  their weights, for the interval  $(0, 1)$ . Then an areal quadrature for  $\Omega$  with  $N = nm$  nodes  $(x_j, y_j)$  and weights  $w_j$  is:

$$(x_{l+(i-1)m}, y_{l+(i-1)m}) = (\alpha_l X_i, \alpha_l Y_i), \quad \text{for } i = 1, \dots, n, \quad l = 1, \dots, m, \quad (11)$$

$$w_{l+(i-1)m} = \alpha_l \tilde{w}_l (X_i V_i - Y_i W_i), \quad \text{for } i = 1, \dots, n, \quad l = 1, \dots, m. \quad (12)$$

This follows by applying (10) and the rule on  $(0, 1)$  to the “dilation” parameterization  $\iint_{\Omega} f \, dx dy = \int_{\partial\Omega} (\int_0^1 f(\alpha \mathbf{x}) \alpha d\alpha) \mathbf{x} \times ds$ , where  $\mathbf{x} \in \partial\Omega$ , and the 2D cross product is understood to give a scalar. The resulting nodes lie along the lines connecting the origin to the boundary nodes, as in Fig. 2(c). If  $\Omega$  is not star-shaped about the origin, then some of the nodes lie outside  $\Omega$  and some  $w_j$  are negative; however, we observe little loss of accuracy unless  $\Omega$  is highly non-convex or poorly centered on the origin.

Finally, we must build a vector line integral rule (10). The simplest case is when  $\partial\Omega$  is parameterized in a counter-clockwise sense over  $t \in [0, 2\pi)$  by a smooth  $2\pi$ -periodic vector function  $\mathbf{x}(t) := (X(t), Y(t))$ . Then

$$\int_{\partial\Omega} \mathbf{f} \cdot ds = \int_0^{2\pi} \mathbf{f}(\mathbf{x}(t)) \cdot \mathbf{x}'(t) dt \approx \sum_{i=1}^n \mathbf{f}(\mathbf{x}(2\pi i/n)) \cdot \frac{2\pi}{n} \mathbf{x}'(2\pi i/n), \quad (13)$$

where we applied the  $n$ -point *periodic trapezoid rule* quadrature with nodes  $t = 2\pi i/n$  and equal weights  $2\pi/n$ . Comparing right-hand sides of (10) and (13), one reads off

$$X_i = X(2\pi i/n), \quad Y_i = Y(2\pi i/n), \quad W_i = \frac{2\pi}{n} X'(2\pi i/n), \quad V_i = \frac{2\pi}{n} Y'(2\pi i/n), \quad i = 1, \dots, n. \quad (14)$$

We apply the above to build a family of areal quadratures for the kite domain with smooth boundary  $(X(t), Y(t)) = (0.5 \cos t + 0.5 \cos 2t, \sin t)$ , shown in Fig. 2. Its maximum radius is  $R \approx 1.13$ . We then show multiple types of error convergence for the proposed method for Fresnel diffraction in Fig. 3. The graphs not labeled “self” (ie, blue, black and green) show absolute error in  $u^{\text{ap}}$  at a single point, using as a reference solution the (converged) NSLI edge integral method in the Appendix. The other “self” convergence (red) graphs show the maximum error in  $u^{\text{ap}}$  over  $10^6$  targets, using the converged values themselves as a reference. The “direct” (blue) simply sums (7) without the fast algorithm. The other graphs test two flavors of proposed NUFFT method—arbitrary targets (t3, + signs) and gridded targets (t1, o signs)—each at two different requested tolerances (6-digit and 12-digit).

In each row of panels, the first shows convergence in  $m$  (“radial” nodes), with fixed  $n$  (boundary nodes), and the second vice versa. The right-most panels image, on a  $M = 1000^2$  point grid, the converged intensity  $|u^{\text{oc}}|^2$ , applying (3) so that  $\Omega$  is an occulter. There are several observations:

- In all cases the convergence is very sudden, as is typical with a spectrally-accurate quadrature rule applied to an oscillatory integrand.
- Comparing the top to the bottom rows, where  $f$  has increased by a factor 10, the converged  $m$  and  $n$  have each become about ten times larger. This matches (6).

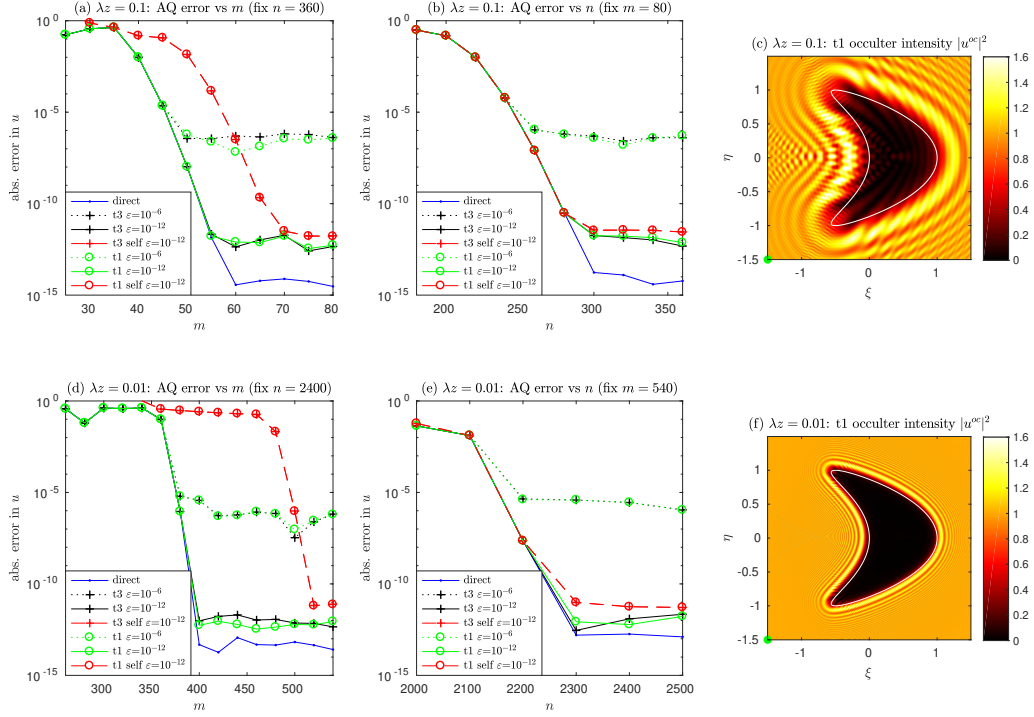


**Fig 3** Convergence of the proposed method for the smooth kite domain (see Sec. 3.1), with respect to  $m$  (“radial” nodes), and  $n$  (boundary nodes). Unless labeled “self”, all errors are measured at the target  $(-3/2, -3/2)$  shown as a green dot in the right-most plots, relative to the reference line integral method (NSLI). Those labeled “self” give the maximum error over  $M = 10^6$  target points relative to their converged values. “direct” (blue) uses (7); “t3” (+ signs) uses the arbitrary-target type 3 NUFFT of Sec. 2.1 (random points lying in  $[-3/2, 3/2]^2$ ), and “t1” (o signs) the grided target type 1 NUFFT of Sec. 2.2 (grid of  $n = 10^3$ ,  $nh = 3$ ). Two NUFFT tolerances  $\varepsilon = 10^{-6}$  and  $\varepsilon = 10^{-12}$  are compared. The occulter Fresnel number for the top row (a–c) is  $f \approx 12.8$ , the bottom (d–f) is  $f \approx 128$ .



$\lambda z$	$f$	$n$ (bdry)	$m$ (radial)	$M$ (targets)	method	median err	max err	CPU time
0.1	12.8	320	—	$10^6$ , random	NSLI	—	—	25.8 s
					BDWF	$2.1e-3$	$1.9e1$	35.2 s
		320	80	$10^6$ , grid	NUFFT t3 ( $\varepsilon=10^{-6}$ )	$6.2e-8$	$1.0e-6$	0.23 s
					NUFFT t3 ( $\varepsilon=10^{-12}$ )	$3.3e-13$	$2.8e-12$	0.32 s
					NUFFT t1 ( $\varepsilon=10^{-6}$ )	$9.6e-9$	$8.0e-7$	0.06 s
					NUFFT t1 ( $\varepsilon=10^{-12}$ )	$1.4e-13$	$2.6e-12$	0.12 s
0.01	128	2400	—	$10^6$ , random	NSLI	—	—	79 s
					BDWF	$1.1e-5$	$1.1e1$	115 s
		2400	560	$10^6$ , grid	NUFFT t3 ( $\varepsilon=10^{-6}$ )	$9.3e-8$	$4.7e-6$	0.29 s
					NUFFT t3 ( $\varepsilon=10^{-12}$ )	$3.4e-13$	$9.5e-12$	0.51 s
					NUFFT t1 ( $\varepsilon=10^{-6}$ )	$2.1e-8$	$4.6e-6$	0.17 s
					NUFFT t1 ( $\varepsilon=10^{-12}$ )	$1.8e-13$	$9.6e-12$	0.21 s
0.001	1280	24000	5600	$10^7$ , random	NUFFT t3 ( $\varepsilon=10^{-6}$ )	$5.2e-8$	$5.3e-6$	16.2 s
				$10^7$ , grid	NUFFT t1 ( $\varepsilon=10^{-6}$ )	$1.9e-8$	$3.7e-6$	10.4 s

**Table 1** Error in  $u^{oc}$  and run times of several methods for the smooth kite occulter with converged quadrature parameters. The domain, upper two  $\lambda z$  choices, and target region are as in Fig. 3. Blank entries in the table to be taken as repeated from above, and “—” indicates not applicable. In both random and grid cases, errors are measured relative to the NSLI reference method (see Appendix). Timings for NSLI and BDWF<sup>15</sup> are not listed for the grid cases since they are identical to the random cases. The last two rows are close to the largest Fresnel number  $f$  that the laptop can handle (errors were checked at only  $10^4$  targets in those cases). See Sec. 3.1 for other details.

- The “direct” application of (7) converges to 13–14 digits, while the NUFFT methods convergence bottoms out at within one digit of the requested  $\varepsilon$ , as expected.
- The “self” convergence (red graphs) in  $n$  (panels b, e) occurs in tandem with the independent error at the single test point  $(-3/2, -3/2)$ . However, for  $m$  (panels a, d) this is not quite true, even though the test point is the point in the target domain  $[-3/2, 3/2]^2$  maximizing the maximum source-target separation  $r$ . This is due to particulars of the angular variation in node density, and reminds one that convergence must be tested at *all* target points.

Table 1 reports CPU timings and errors for these same tasks at converged  $n$  and  $m$  quadrature parameters. NSLI (known to achieve 13–14 digits with these parameters) is used as the reference for all errors. A state of the art edge integral code, BDWF<sup>15</sup> (as available in SISTER,<sup>26</sup> and documented in<sup>33</sup>) is also tested with the same  $n$ : while its median errors are as expected from its use of a 2<sup>nd</sup>-order accurate midpoint rule, its maximum errors are larger than 1. These huge errors appear to be confined to a few target points very near  $\partial\Omega$ , the geometric shadow edge. The main conclusions from Table 1 are then:

- In this setting, the proposed NUFFT based methods are 100 to 300 times faster than the edge integral methods (for arbitrary targets), or 400 to 600 times faster (for gridded targets).
- The proposed methods *robustly* (uniformly at all targets) achieve close to the requested error.
- At the largest  $\lambda z$  ( $f \approx 12.8$ ), the t1 achieves  $\sim 10^7$  targets/second, and the t3 achieves  $\sim 4 \times 10^6$  targets/second, with only a weak dependence on tolerance. These are only slightly slower for  $f$  ten times larger.

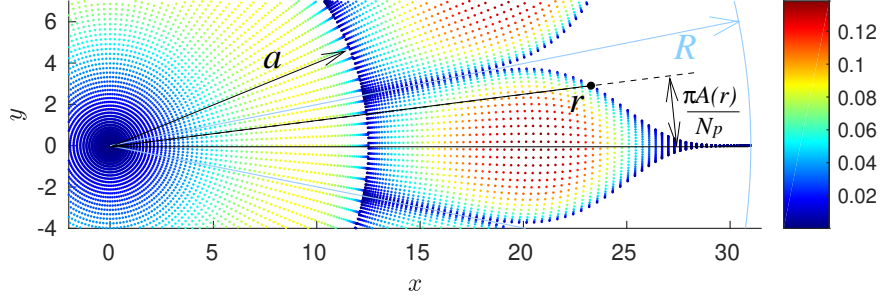


**Fig 4** Idealized starshade geometry (zoom for clarity).  $A(r)$  is the apodization profile controlling petal angular width, here illustrated with the HG (offset hyper-Gaussian<sup>14</sup>) with  $N_p = 16$  petals. The colored dots show areal quadrature nodes  $(x_j, y_j)$  with weights  $w_j$  indicated by color as in the colorbar.  $m = 80$  Gauss radii cover the petal length, with  $n_p = 30$  Gauss nodes covering the petal angular width at each radius.

- At the smallest  $\lambda z = 10^{-3}$  ( $f \approx 1280$ ) the asymptotic  $\mathcal{O}(f^2 \log f)$  cost has started to dominate. Note that 134 million nodes are being mapped to 10 million targets in around 10 seconds.

Since under the hood the NUFFT uses FFTs, the reader might worry about their RAM usage. It is very mild: for t1 (gridded) cases the FFT size is  $5/4$  times (for  $\varepsilon \geq 10^{-9}$ , or twice otherwise) the requested grid size, in each dimension. For t3, FFT dimensions scale like  $f$ : for the smallest  $f \approx 12.8$ , the FFT is a tiny  $216 \times 288$ . This is to be compared with the  $32768 \times 32768$  FFT needed for a sub-pixel sampling method to reach around 6-digit accuracy in  $u$  in various tests<sup>17</sup> at similar  $f$ . In the penultimate row of the table  $f$  is  $10^2$  times larger, yet the FFT is only  $7500 \times 9600$  (similar to the maximum  $r^2/\lambda z \approx 8900$  zones), and total RAM usage is 17 GB, about the largest the laptop can handle.

### 3.2 Application to starshade modeling

Idealized starshades are described<sup>10,14,15</sup> by a radial apodization function  $A(r)$ , where (in this section only) we use  $(r, \theta)$  as occulter-plane polar coordinates about the origin.  $A(r)$  is 1 (indicating a fully blocking disc) for  $r < a$ , and drops in a carefully optimized fashion in  $r \in [a, R]$  to close to zero at  $R$ , the maximum occulter radius, and identically 0 beyond this. Apodization over  $[a, R]$  is realized via  $N_p$  identical binary petals, each of whose angular width at radius  $r$  is  $2\pi A(r)/N_p$ . Let the function  $P(\alpha)$  denote  $\alpha + 2\pi n$  for the unique  $n \in \mathbb{Z}$  such that  $\alpha + 2\pi n \in [-\pi, \pi)$ , a common definition of the principal value of an angle. Then the occulter is the “flower” shape,

$$\Omega = \left\{ (r, \theta) : 0 \leq r \leq R, P(N_p \theta) \in (-\pi A(r), \pi A(r)) \right\}. \quad (15)$$

See Fig. 4. Note that published  $A(r)$  designs are *discontinuous* at  $a$  (indicating a gap between petals), and at  $R$  (petal tips have finite width). In early “analytic” designs these discontinuities were required to be no larger than about  $10^{-5}$  in size to minimize Arago-spot-style diffraction into the deep shadow [14, §4.3], but designs generated by optimization over a  $\lambda z$  band<sup>10,26</sup> have much larger gap and tip discontinuities, of order  $10^{-2}$  to  $10^{-3}$ , whose Arago effect is apparently cancelled out by distributed “ripples” [14, §5] in  $A(r)$ .

Recall that the task is simply to evaluate (1) and (3) with errors in  $u^{\text{oc}}$  no worse than  $10^{-6}$ . To apply the proposed method, we build a high-order areal quadrature as follows. Since  $A(r)$  is discontinuous at  $r = a$ , we split  $\Omega$  into the disc of radius  $a$  plus each of  $N_p$  petals. Our disc

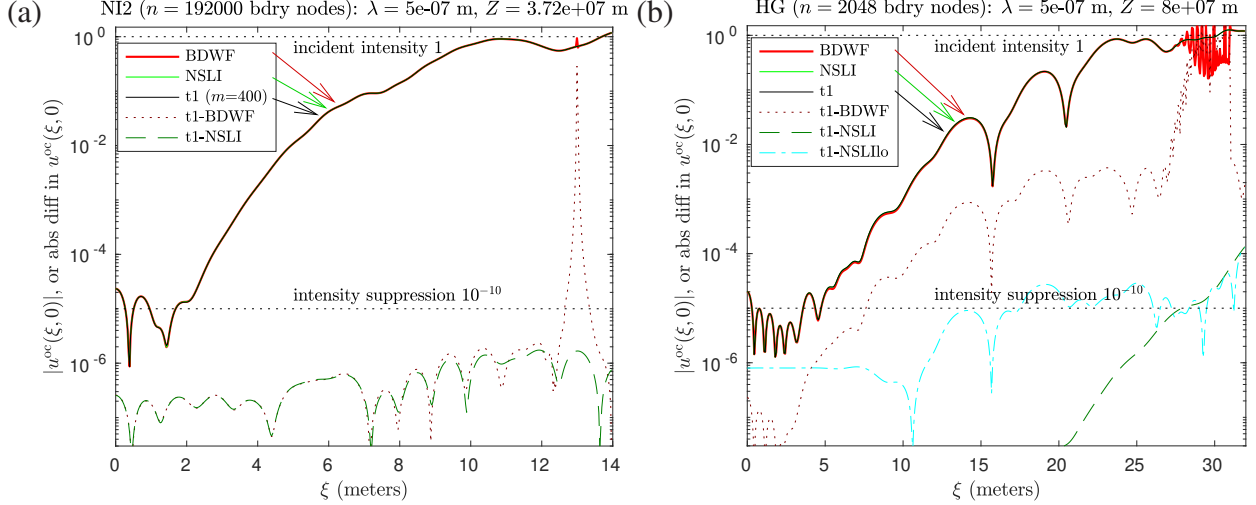


**Fig 5** Validation of diffracted  $u^{\text{oc}}$  along a radial slice for two starshade designs: NI2 (optimized function with ripples<sup>16</sup>) and HG (offset hyper-Gaussian analytic function<sup>14</sup>). Both have  $N_p = 16$  petals. The proposed NUFFT t1 method (black line) is compared against edge-integral methods BDWF (red) and NSLI (green). Labels such as “t1-BDWF” indicate the absolute difference in  $u^{\text{oc}}$  between two methods. BDWF and NSLI use the same boundary nodes, except for “NSLIlo” which uses  $10\times$  the boundary nodes and  $2^{\text{nd}}$ -order weights. For details see Sec. 3.2.

quadrature simply applies (11)–(12) to the uniform  $n_d$ -node line integral on its boundary, that is, (14) applied to the parameterization  $(X(t), Y(t)) = (a \cos t, a \sin t)$ . We use  $m_d$  radial nodes. We then cover each petal by  $m$  nodes in the radial direction, then cover the arc at each of these node radii by  $n_p$  nodes, as in Fig. 4. Specifically, let  $\{r_l, \hat{w}_l\}_{l=1}^m$  be 1D Gauss–Legendre nodes and weights for  $(a, R)$ , and  $\{t_i, \hat{w}'_i\}_{i=1}^{n_p}$  be similar nodes and weights for  $[-\pi/N_p, \pi/N_p]$ . Then the areal nodes (in Cartesians) and weights for one petal are

$$\begin{aligned} (x_{l+(i-1)m}, y_{l+(i-1)m}) &= (r_l \cos(A(r_l)t_i), r_l \sin(A(r_l)t_i)), & \text{for } i = 1, \dots, n_p, l = 1, \dots, m, \\ w_{l+(i-1)m} &= r_l \hat{w}_l A(r_l) \hat{w}'_i, & \text{for } i = 1, \dots, n_p, l = 1, \dots, m. \end{aligned}$$

Other petals are obtained by rotation by multiples of  $2\pi/N_p$ . The total number of nodes is then  $N = n_d m_d + N_p n_p m$ . We will fix  $m_d = m$  and  $n_d \approx 0.3 N_p n_p$ , leaving two (petal) convergence parameters  $m$  and  $n_p$ .

### 3.2.1 Accuracy validation

We compare in Fig. 5 the wave amplitudes along a radial slice computed by three methods, for two designs of starshade: “NI2” (a small occulter with rippled profile optimized for a blue-green  $\lambda$  range<sup>16</sup>), and “HG” (a large occulter with analytic “offset hyper-Gaussian” profile<sup>14</sup>). We choose  $\lambda$  within their designed wavelength windows. The parameters used, and some CPU timings, are listed in Table 2. Since they have different geometry descriptions, we treat the two designs in turn.

**NI2.** The optimized profile  $A(r)$  is available in the SISTER package<sup>26</sup> in the form of 2462 equispaced samples covering the petal radius range  $[a, R] = [5, 13]$  m. From these, we use piecewise cubic splines to interpolate  $A$  at  $m$  radial Gauss nodes in  $[a, R]$ . Since  $A''(r)$  appears to have at least 13 “bang-bang” type discontinuities (the discrete  $2^{\text{nd}}$  derivative mostly takes values  $\pm\sigma$ , for some constant  $\sigma$ , or 0), this *necessarily* limits accuracy to around 6-7 digits. By a convergence

design	$\lambda$ (m)	$z$ (m)	$f$	$m$ (petal)	total nodes	$M$ (targets)	method	CPU time
NI2	5e-7	3.72e7	9.1	6000	$n=192000$	$10^6$ , grid	BDWF	5361 s
				400	$N=499200$		NUFFT t1 ( $\varepsilon=10^{-8}$ )	0.076 s
HG	5e-7	8e7	24	60	$n=2048$	$10^6$ , grid	BDWF	80.5 s
				60	$N=37440$		NUFFT t1 ( $\varepsilon=10^{-8}$ )	0.042 s

**Table 2** Parameters and CPU times for the proposed NUFFT t1 and the BDWF edge-integral to complete the same diffraction tasks, for two starshades. See Fig. 5 for comparisons of their answers. The Fresnel number  $f$  uses the maximum radius  $R$  in (2).  $N$  is the number of areal quadrature nodes, while  $n$  the number of boundary nodes.

study we found that  $m = 400$ , and  $n_p = 40$  nodes across each petal, were sufficient for areal quadrature to match this accuracy. For BDWF we used the  $n = 192000$  boundary nodes as given and used in SISTER. These have 6000 nodes per petal edge, but no nodes covering the inter-petal gaps, or tips (each of which is 0.03 m wide). For NSLI we used an  $n$ -node vector line integral quadrature matching the 2<sup>nd</sup>-order accurate midpoint rule in BDWF (this match was needed to accurately handle the wide tips with a single segment). Fig. 5(a) shows that the proposed NUFFT t1 method matches both of these edge integral methods to around  $3 \times 10^{-7}$  in  $u^{oc}$  in the shadow region where  $|u^{oc}| \leq 2 \times 10^{-5}$ . NSLI agrees with t1 to around 6-digits everywhere. However, at  $\xi \approx 13$  m, the error of BDWF spikes to  $\mathcal{O}(1)$  as  $(\xi, 0)$  approaches  $\partial\Omega$ .

**Remark 3.** *Since  $z/\lambda \sim 10^{14}$ , overall phase is meaningless, thus we fit the phase of BDWF to the other two methods at a single target. We then quote absolute differences in complex  $u^{oc}$ . This is a more predictable metric than the error in intensity  $|u^{oc}|^2$ , which is affected by local intensity.*

**HG.** Here the profile is analytically known<sup>14</sup>:  $A(r) = e^{-[(r-a)/b]^p}$  in  $[a, R]$ , where  $a = b = 12.5$  m, the maximum radius is  $R = 31$  m, and  $p = 6$ . A convergence study shows that only  $m = 60$  and  $n_p = 30$  are needed, giving an areal quadrature of  $N = 37440$  nodes. For NSLI we used  $A(r)$  and  $A'(r)$  to generate a high-order line integral quadrature using the same  $m = 60$  radii per petal, plus four Gauss nodes across each gap and tip, giving  $n = 2048$  in total (see `starshadeliquad` in our repository<sup>33</sup>). We also fed these boundary nodes (but of course not their high-order weights) to BDWF. Fig. 5(b) shows that the three methods again agree to the desired accuracy almost everywhere, apart from BDWF near  $\partial\Omega$  where again its errors hit  $\mathcal{O}(1)$ .

**Remark 4.** *For HG with  $m = 60$  the errors of BDWF are summarized by 2-3 digits of relative accuracy overall, giving 6-7 digits of absolute  $u^{oc}$  accuracy in the deep shadow. Yet NSLI, if fed the low-order midpoint rule used inside BDWF, gives only 4-digit absolute accuracy, thus is useless in deep shadow. Fig. 5(b) thus also explores (dash-dot line) the errors of NSLI with this low-order rule and the larger  $m = 600$ : the absolute error now bottoms out at a useful  $10^{-6}$ . This highlights an advantage of BDWF over plain NSLI when deep shadows are modeled with poor quadrature, a subtle point explained in Remark 5.*

### 3.2.2 Solution speed

Table 2 presents CPU times for the above converged experiments on gridded targets (we omit NSLI times since they are similar to BDWF.) We make the following observations:

- For NI2 our proposal is around  $70000\times$  faster, and for HG around  $2000\times$  faster, than a state-of-the-art edge integral method.

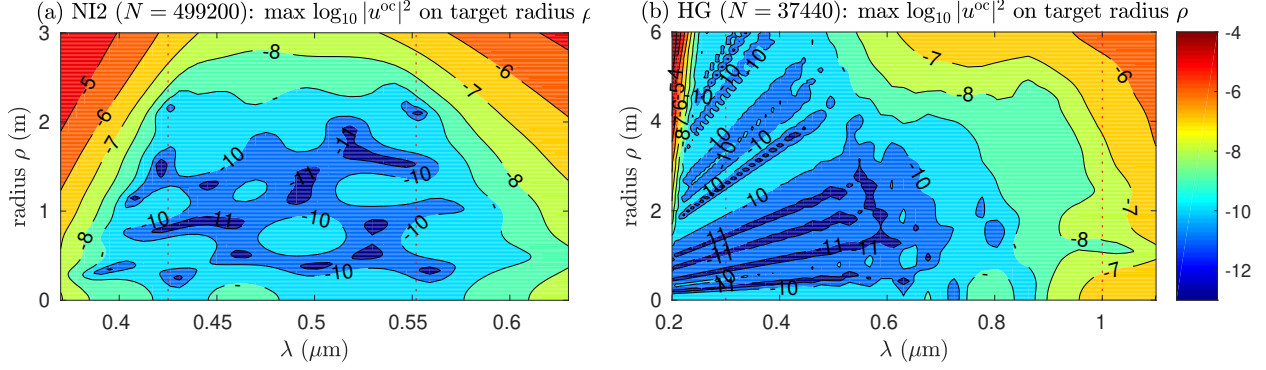


**Fig 6** Intensity (on  $\log_{10}$  scale indicated on the right) as a function of wavelength and target radius  $\rho$  from the center, for the two starshade designs (NI2 and HG) of Fig. 5. At each of 200  $\rho$  values, the maximum over 300 angles is taken. The incident intensity is 1. The NUFFFT t3 method is used. Vertical dotted lines show the designed  $\lambda$  range.

- By reinterpolation of the NI2 profile, and code changes to use a high-order quadrature, BDWF could probably be sped up by a factor of 15. BDWF is found also to gain a factor of about two when multiple  $\lambda$  are needed. Neither factor impacts the conclusions much.
- Since the number  $N$  of areal nodes is smaller than the large number  $M$  of targets, the cost of the NUFFFT method is almost independent of  $N$ , hence of the starshade complexity, or  $f$ .

We now turn to arbitrary targets. In Fig. 6 the intensity suppression of the two starshade designs are studied, sweeping 50 wavelengths, and taking the maximum intensity  $|u^{oc}|^2$  over circles of varying radius  $\rho$  ( $M = 60000$  targets at each  $\lambda$ ), using the proposed NUFFFT t3 method. The narrow-band nature of NI2, and deterioration of HG above  $0.8 \mu\text{m}$ , are apparent. The entire calculation for both starshades totals 6 seconds on the laptop.

Finally, we report initial timing results upon having (rather crudely) inserted the NUFFFT t3 method in place of BDWF within the SISTER code base.<sup>26</sup> (See `sister_mods` in our repository.<sup>33</sup>) Running a standard SISTER “PSF basis” generation task for the non-spinning NI2 starshade, 14 wavelengths are needed covering  $[0.425, 0.555] \mu\text{m}$ , at each of which  $M = 806144$  targets are needed. (Targets are organized into  $16 \times 16$  telescope pupil grids, translated to 3149 different  $(\xi, \eta)$  centers covering a sector with angle  $2\pi/N_p$ .) We had to reorganize the loop ordering, since BDWF was called separately for each pupil while grouping wavelengths together for speed, whereas the NUFFFT t3 is most efficient with a *single call to all targets* at each wavelength.

The original SISTER run time was an estimated 6.5 hours (since BDWF gets about  $6 \times 10^7$  node-target pairs per second). The NUFFFT t3 method, using parameters as in the previous section, took 2.6 seconds. The acceleration is thus about  $10000\times$ .

### 3.3 A complicated domain

As a final example we compute Fresnel diffraction for an aperture with fractal boundary, specifically the standard Koch snowflake with maximum radius  $R = 1$ . Let  $\Omega_0$  denote the equilateral triangle with side length  $\sqrt{3}$ ,  $\Omega_1$  its union with the three triangles of side  $\sqrt{3}/3$ ,  $\Omega_2$  the union of  $\Omega_1$  with the 12 triangles of side  $\sqrt{3}/9$ , etc, so that  $\Omega_L$  is the level- $L$  construction; see Fig. 7(a). To reach level  $L = 13$ ,  $n_{\text{tri}} = 1 + 3 \sum_{k=0}^{L-1} 4^k = 67108864$  triangles are needed. To build an areal quadrature, the integral over each triangle is approximated by a simple  $p \times p$  node product

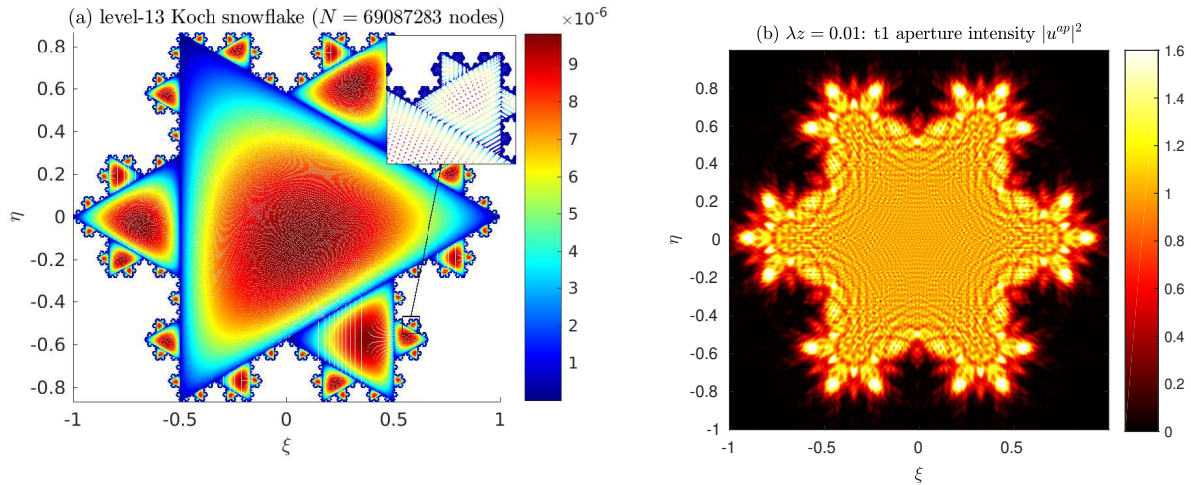


**Fig 7** Koch fractal aperture diffraction example from Sec. 3.3. (a) shows the areal quadrature constructed by a union of about 67 million triangles. The color of each node  $(x_j, y_j)$  indicates its weight  $w_j$  using the scale on the right. The inset shows a zoom into the region shown, resolving individual nodes. (b) shows intensity (on  $\log_{10}$  scale indicated on the right) computed on a million-point grid by the t1 NUFFT method in under 5 seconds.

Gauss–Legendre quadrature, by translating one vertex to the origin then applying (11)–(12) to the discretized line integral connecting the other two vertices (see inset of figure). To accurately handle the oscillatory integrand as in (6), the node spacing should not exceed  $\mathcal{O}(1/f)$ ; thus we designed a heuristic choice of  $p$  that varied from 217 for the largest triangle to  $p = 1$  at levels  $L \geq 10$ , and checked  $p$ -convergence for Fresnel integrals for  $\lambda z \geq 0.01$ . For  $\Omega_{13}$ , the resulting total node number  $N$  is about 69 million, requiring about 4 minutes to build in our simple implementation.

The t1 NUFFT method with  $\varepsilon = 10^{-6}$  is then applied to this areal quadrature, to resolve the diffracted field for  $\lambda z = 0.01$  on a grid of  $10^6$  target points, giving Fig. 7(b). For each new  $\lambda z \geq 0.01$  this takes 4.6 seconds. Since  $\Omega_{13}$  has  $3 \cdot 4^{13} \approx 2 \times 10^8$  edges, an edge integral method of similar accuracy is estimated to be around  $10^5$  to  $10^6 \times$  slower. We have checked (via  $p$ -convergence at each level) that  $u$  computed for  $\Omega_{13}$  has at least 6-digit accuracy.

However, we may also interpret the calculation as an approximation to one for the *limit domain*  $\Omega_\infty$  with true fractal boundary. Since the smallest triangles in  $\Omega_{13}$  have side  $1.1 \times 10^{-6} \ll \lambda z$ , ie, much smaller than any Fresnel zone, we are well into the regime of Richardson extrapolation in  $L$ , with differences from the limit scaling like  $(4/9)^L$ . The largest absolute change in  $u$  on the grid in going from  $\Omega_{12}$  to  $\Omega_{13}$  was  $1.6 \times 10^{-4}$ , thus, by extrapolation, the largest change in  $u$  between  $\Omega_{13}$  and the limiting domain  $\Omega_\infty$  is around 4/5 of this. Thus we may quote uniformly about 4-digit accuracy for diffraction from the limit fractal domain. (By applying Richardson to a sequence one could in fact get many more digits without much extra effort.)

## 4 Conclusion and discussion

We have explained a fast algorithm for Fresnel diffraction from binary aperture or occulter shapes, which achieves high accuracy via flexible areal quadrature schemes over the planar domain, yet speeds close to regular-grid FFT propagation methods, via the nonuniform FFT. Extensive tests of error convergence and CPU timings show between 2 and 5 orders of magnitude acceleration over edge integral methods at comparable accuracies. Thus, at moderate Fresnel numbers  $f \leq 10^2$

one can evaluate accurate diffraction fields from complicated shapes such as starshades almost instantaneously (0.1 seconds for a grid of  $10^6$  targets). For higher  $f$ , the  $\mathcal{O}(f^2 \log f)$  cost starts to dominate. RAM usage starts to become a limitation only at  $f \sim 10^3$ . Along the way, we have reformulated edge integrals as a non-singular line integral that is numerically robust (Appendix A).

Although we did not exploit it, the proposed NUFFT method can trivially include continuous phase/amplitude variations at the areal nodes, while retaining accurate edge diffraction. This is impossible for traditional edge integral methods, but we note exciting recent progress on including low-frequency phase variations with edge integrals [17, Sec. 6].

Our findings highlight the importance of high-order accurate quadratures, both for line integrals and, crucially, planar integrals. We have shown how the latter may be easily constructed for three classes of domain  $\Omega$  (smooth, starshades, and unions of triangles). Such construction on a case-by-case basis is possible, at least up to the tolerance with which a description of  $\partial\Omega$  is available. Yet to automate this procedure for a requested accuracy and  $f$ , given “any”  $\Omega$ , raises 2D geometry representation and meshing issues common throughout engineering and scientific computing. This is a huge topic with many available tools. Given the benefits that we show in optical modeling, automated high-order areal quadratures from CAD formats should be a useful future project.

Other fruitful directions to extend the work include:

- For starshades, this tool opens up the rapid Monte Carlo study of the effects of manufacturing and in-flight variations upon optics.<sup>16</sup> While this could be done simply by piggybacking off edge quadratures, realistic nonsymmetric starshade areal quadrature generation would help.
- Further acceleration is probable by drop-in replacement of FINUFFT by a GPU library.
- It seems that a NUFFT replacing the first FFT in method (a)(i) from the Introduction could enable efficient new “angular spectrum of plane waves” [6, §3.10] (one-way Helmholtz) methods for binary aperture diffraction beyond the Fresnel regime.

## Acknowledgments

This work benefited from discussions with David Spergel, Robert Vanderbei, Stuart Shaklan, and Eric Cady. The Flatiron Institute is a division of the Simons Foundation.

## Appendix A: Fresnel edge integral methods—equivalence and desingularization

### A.1 Equivalence of edge integral methods for planar waves and apertures

Dauger<sup>19</sup> noticed that, by using polar coordinates about the target  $(\xi, \eta)$ , ie,  $x = \xi + r \cos \theta$  and  $y = \eta + r \sin \theta$ , the Fresnel aperture integral (1) may be analytically integrated in  $r$ , for each  $\theta$ , as follows. Assuming that the target is in  $\Omega$  (geometric shadow), furthermore that  $\Omega$  is strictly star-shaped about this target, (1) becomes

$$u^{\text{ap}}(\xi, \eta) = \frac{1}{i\lambda z} \int_0^{2\pi} \int_0^{R(\theta)} e^{\frac{i\pi}{\lambda z} r^2} r dr d\theta = \frac{-1}{2\pi} \int_0^{2\pi} [e^{\frac{i\pi}{\lambda z} R(\theta)^2} - 1] d\theta \quad (16)$$

where  $R(\theta)$  is the distance  $r$  where the in-plane ray launched at angle  $\theta$  from the target exits  $\Omega$ . If these conditions are broken,  $R(\theta)$  becomes multi-valued. For targets outside  $\Omega$ , the second term in square brackets must be replaced by one similar to the first but involving the  $r$  value where the ray

first enters  $\Omega$ . The resulting numerical method is cumbersome for a general  $\Omega$  because much effort is spent finding, and tracking as a function of  $\theta$ , these multiple ray intersection points.<sup>19</sup>

It is simpler to reformulate (1) in terms of a line integral over  $\partial\Omega$ . Cash [14, (46)] provides such a formula but no rigorous derivation. To remedy this, fixing the target, we write  $\mathbf{r} := (x - \xi, y - \eta)$ , hence  $r^2 = \|\mathbf{r}\|^2$ , and define the 2D vector field

$$\mathbf{F}(x, y) := \frac{-1}{2\pi} \frac{\mathbf{r}}{r^2} e^{\frac{i\pi}{\lambda z} r^2}, \quad (x, y) \neq (\xi, \eta). \quad (17)$$

After cancelling terms, its divergence is found to be simply the Fresnel integrand from (1) minus the unit 2D delta distribution at the target (the latter can be proven by excluding a small disk of radius  $r \rightarrow 0$  about the target). That is,

$$\nabla \cdot \mathbf{F}(x, y) = \frac{1}{i\lambda z} e^{\frac{i\pi}{\lambda z} r^2} - \delta(\mathbf{r}). \quad (18)$$

Applying the divergence theorem in  $\Omega$ , with  $\mathbf{n}$  the unit outward normal, and, as before, the 2D cross product taken to be a scalar,

$$\iint_{\Omega} \nabla \cdot \mathbf{F} \, dx dy = \int_{\partial\Omega} \mathbf{F} \cdot \mathbf{n} \, ds = \int_{\partial\Omega} \mathbf{F} \times ds = \frac{-1}{2\pi} \int_{\partial\Omega} e^{\frac{i\pi}{\lambda z} r^2} \frac{\mathbf{r} \times ds}{r^2}.$$

Substituting (18) and recalling (1) gives the line integral formula

$$u^{\text{ap}}(\xi, \eta) = \frac{-1}{2\pi} \int_{\partial\Omega} e^{\frac{i\pi}{\lambda z} r^2} \frac{\mathbf{r} \times ds}{r^2} + u_{\text{geom}}^{\text{ap}}(\xi, \eta), \quad \text{where } u_{\text{geom}}^{\text{ap}}(\xi, \eta) := \begin{cases} 1, & (\xi, \eta) \in \Omega \\ 0, & \text{otherwise} \end{cases} \quad (19)$$

This is easily seen to be equivalent to Dauger's formulae using the facts: i)  $d\theta = (\mathbf{r} \times ds)/r^2$ , ii)  $u_{\text{geom}}^{\text{ap}}(\xi, \eta) = \int_0^{2\pi} d\theta/2\pi$ , and iii) the multiple values of  $R(\theta)$  correspond to  $\theta$  folding back as  $\partial\Omega$  is traversed.

We now show that, within the Fresnel approximation, the Miyamoto–Wolf [25, Eqs. (5.1), (5.5)] boundary diffraction wave (BDW) formulation used by Cady<sup>15</sup> is also equivalent to the above. Given  $u(x, y)$ , the plane incident wave at the aperture with unit direction vector  $\mathbf{p}$ , this states (noting that our  $u^{\text{ap}}$  definition excludes the phase of plane  $z$ -propagation),

$$u^{\text{ap}}(\xi, \eta) = \frac{1}{4\pi} e^{-2\pi iz/\lambda} \int_{\partial\Omega} u(x, y) \frac{e^{2\pi i\rho/\lambda}}{\rho} \frac{\hat{\boldsymbol{\rho}} \times \mathbf{p} \cdot ds}{1 + \hat{\boldsymbol{\rho}} \cdot \mathbf{p}} + u_{\text{geom}}^{\text{ap}}(\xi, \eta). \quad (20)$$

Here we recall that  $\rho = \sqrt{r^2 + z^2}$  is the target-source 3D distance, and define  $\hat{\boldsymbol{\rho}}$  to be the unit vector pointing from target to source ( $\rho$  is notated as  $s$  in standard references, but we reserve the latter for arclength). Since we are concerned with planar incidence,  $u(x, y) \equiv 1$  and  $\mathbf{p} = (0, 0, 1)$ . Since  $r \ll z$  is implicit in (1), we insert the leading-order small-angle approximations  $\rho \approx z$ ,  $\hat{\boldsymbol{\rho}} \times \mathbf{p} \cdot ds \approx (\mathbf{r} \times ds)/z$ ,  $1 + \hat{\boldsymbol{\rho}} \cdot \mathbf{p} \approx r^2/(2z^2)$ , and the usual Fresnel approximation  $e^{2\pi i\rho/\lambda} \approx e^{2\pi iz/\lambda} e^{\frac{i\pi}{\lambda z} r^2}$ . The result is precisely (19). Thus all three edge formulations are equivalent.

However, it is worth noting that BDW (20) and some formulae in Dubra–Ferrari<sup>21</sup> have a wider range of validity than (1), Dauger's formulae, or (19), since they allow out-of-plane apertures and more general incident waves.



## A.2 A robust non-singular line integral (NSLI) formulation

To our knowledge all edge integral numerical codes use formulae shown in the previous section to be equivalent to (19), and are thus well known to be plagued by two serious problems:<sup>14, 15, 17, 19, 21</sup>

1. targets must be labeled as being inside or outside of  $\Omega$  in a robust fashion, no matter how close they are to  $\partial\Omega$ , otherwise  $\mathcal{O}(1)$  errors result, and
2. when the target approaches  $\partial\Omega$ , the integrand on  $\partial\Omega$  becomes nearly singular, requiring increasingly refined quadrature near the target to retain accuracy. (Dauger’s  $\theta$ -parameterization conceals this, but does not remove the difficulty, since  $R(\theta)$  changes arbitrarily rapidly.)

For instance, in Sec. 3.1 and 3.2.1 we saw that the BDWF code loses all accuracy near to  $\partial\Omega$ . However, once it is realized that the two problems are in fact facets of the same phenomenon, they can be made to “cancel out”.

This works as follows. It is well known [40, (6.23)] (or combining facts i) and ii) above), that

$$u_{\text{geom}}^{\text{ap}}(\xi, \eta) = \frac{1}{2\pi} \int_{\partial\Omega} \frac{\mathbf{r} \times d\mathbf{s}}{r^2}. \quad (21)$$

Inserting this into (19) gives *one formula which applies whether the target is inside or outside  $\Omega$ ,*

$$u^{\text{ap}}(\xi, \eta) = \frac{1}{2\pi} \int_{\partial\Omega} [1 - e^{\frac{i\pi}{\lambda z} r^2}] \frac{\mathbf{r} \times d\mathbf{s}}{r^2} \quad (\text{NSLI formula}). \quad (22)$$

This has no singularity as  $r \rightarrow 0$  (target approaching  $\partial\Omega$ ) because the term in square brackets is  $\mathcal{O}(r^2)$ , cancelling the denominator. The integrand is as smooth as the Fresnel zones, ie, as smooth as the diffracted field in the target plane. We believe that (22) is new.

This leads to an incredibly simple yet robust code. For instance, in MATLAB, if `bx` and `by` list coordinates of nodes on  $\partial\Omega$ , with `wx` and `wy` the corresponding weights for a vector line integral as in Sec. 3.1, the entire NSLI code to output  $u^{\text{ap}}$  at a target `(xi, eta)` is five lines:

```
rx = bx - xi; ry = by - eta;           % components of r displacement vector
r2 = rx.*rx + ry.*ry;                 % r^2
f = (1 - exp((1i*pi/lambdaz)*r2)) ./ r2;
f(r2==0.0) = 0.0;                     % kill NaNs (target hits a node)
uap = sum((rx.*wy - ry.*wx) .* f) / (2*pi); % cross product, quadrature
```

There is a subtlety here: numerical eyebrows should immediately be raised because `f` involves *catastrophic cancellation* as  $r \rightarrow 0$  when the target approaches a node. We now apply forward error analysis [41, Ch. 1]. To understand why the cancellation is in fact barely a problem, one has to treat the real and imaginary parts separately (not doing so leads to a pessimistic prediction).

The imaginary part of the `exp` is  $\sin((\pi/\lambda z)r^2)$ , which, given a rounded value of `r2`, is computed to *relative* accuracy  $\mathcal{O}(\epsilon_{\text{mach}})$ , where  $\epsilon_{\text{mach}} \approx 1.1 \times 10^{-16}$  is the usual double precision relative error. Subtraction from 1 does not change the imaginary part. The division by `r2` then results in absolute error  $\mathcal{O}(\epsilon_{\text{mach}})$ , which then gets multiplied by the  $\mathcal{O}(r)$  cross product, giving  $\mathcal{O}(\epsilon_{\text{mach}}r)$ . Note that this holds even though `r2` is necessarily inaccurate due to coordinate subtraction in line 1.

Now to the real part of the  $\text{exp}$ , which is  $1 + \mathcal{O}(r^4)$ . Thus when  $r \lesssim \epsilon_{\text{mach}}^{1/4}$ , the real part of  $\text{exp}$  is in machine arithmetic *exactly* 1, which cancels the other 1 exactly, leaving zero. Since the true answer is  $\mathcal{O}(r^3)$ , in this regime the final error is bounded by  $\mathcal{O}(\epsilon_{\text{mach}}^{3/4})$ . On the other hand, for  $r \gtrsim \epsilon_{\text{mach}}^{1/4}$ , catastrophic cancellation occurs: the error in the real part of  $\text{exp}$  is  $\mathcal{O}(\epsilon_{\text{mach}})$ , so the final error is  $\mathcal{O}(\epsilon_{\text{mach}}/r)$ . In summary, uniformly in  $r$ , the final error is bounded by  $\mathcal{O}(\epsilon_{\text{mach}}^{3/4})$ . In practice, we find by comparison to the areal quadrature answers that this uniform bound is around  $10^{-14}$ , which is adequate. Replacing by Taylor expansions for small  $r$  could possibly gain a digit.

The formula (22), in the form of the above code looped over target points, serves as our reference direct method. A documented, tested MATLAB/Octave implementation is in the repository<sup>33</sup> in `bdrymeths/nsli_pts.m`

**Remark 5.** When a poor quadrature (that is, low order and few nodes) is used with deep shadow regions, the usual line integral (19) has one advantage over NSLI (22): it can in shadows achieve relative accuracy in  $u$ , appropriate to the quadrature, because  $u_{\text{geom}} = 0$  exactly. NSLI merely achieves absolute accuracy in  $u$ , thus may require a better quadrature to resolve deep shadows than (19) (as implemented by, eg, BDWF). In essence,  $u_{\text{geom}}^{\text{ap}} \approx 1$  (the “1” term in (22)) to limited accuracy, which is then poorly canceled in (3). To remedy this, our NSLI implementation also includes a flag to use (19) for targets far from  $\partial\Omega$ , combining the robustness of (22) with the deep shadow relative accuracy of BDWF.

## References

- 1 M. Born and E. Wolf, *Principles of Optics*, Pergamon Press, Oxford, 6th ed. (1980).
- 2 P. M. Morse and K. U. Ingard, *Theoretical Acoustics*, McGraw-Hill (1968).
- 3 M. D. Perrin, R. Soummer, E. M. Elliott, *et al.*, “Simulating point spread functions for the James Webb Space Telescope with WebbPSF,” in *Space Telescopes and Instrumentation 2012: Optical, Infrared, and Millimeter Wave*, M. C. Clampin, G. G. Fazio, H. A. MacEwen, *et al.*, Eds., **8442**, 1193 – 1203, International Society for Optics and Photonics, SPIE (2012).
- 4 Y. Hu, Z. Wang, X. Wang, *et al.*, “Efficient full-path optical calculation of scalar and vector diffraction using the Bluestein method,” *Light Sci. Appl.* **9**(1), 119 (2020).
- 5 A. J. Bourdillon, C. B. Boothroyd, J. R. Kong, *et al.*, “A critical condition in Fresnel diffraction used for ultra-high resolution lithographic printing,” *J. Phys. D* **33**(17), 2133–2141 (2000).
- 6 J. W. Goodman, *Introduction to Fourier Optics*, McGraw-Hill, 2nd ed. (1996).
- 7 M. Ruiz-Lopez, A. Faenov, T. Pikuz, *et al.*, “Coherent X-ray beam metrology using 2D high-resolution Fresnel-diffraction analysis,” *J. Synchrotron Rad.* **24**(1), 196–204 (2017).
- 8 T. D. Mast, “Fresnel approximations for acoustic fields of rectangularly symmetric sources,” *J. Acoust. Soc. Am.* **121**, 3311–3322 (2007).
- 9 P. Tsang, T.-C. Poon, W.-K. Cheung, *et al.*, “Computer generation of binary Fresnel holography,” *Appl. Opt.* **50**(7), B88–B95 (2011).
- 10 R. J. Vanderbei, E. J. Cady, and N. J. Kasdin, “Optimal occulter design for finding extrasolar planets,” *Astrophys. J.* **665**(1), 794–798 (2007).
- 11 D. Serre, “The Fresnel imager: instrument numerical model,” *Exp. Astron.* **30**, 111–121 (2011).
- 12 R. Wilhem and K. Laurent, “Improvements on Fresnel arrays for high contrast imaging,” *Exp. Astron.* **45**, 21–40 (2018).

- 13 A. S. Lo, T. Glassman, and C. Lillie, “New Worlds Observer optical performance,” *Proc. SPIE* **6687**, 668716–1 to –9 (2007).
- 14 W. Cash, “Analytic modeling of starshades,” *Astrophys. J.* **738**(1), 76 (2011).
- 15 E. J. Cady, “Boundary diffraction wave integrals for diffraction modeling of external occulters,” *Opt. Express* **20**(14), 15196–15208 (2012).
- 16 S. B. Shaklan, L. Marchen, and E. Cady, “Shape accuracy requirements on starshades for large and small apertures,” in *Techniques and Instrumentation for Detection of Exoplanets VIII*, S. Shaklan, Ed., **10400**, 509–518, International Society for Optics and Photonics, SPIE (2017).
- 17 A. Harness, S. Shaklan, W. Cash, *et al.*, “Advances in edge diffraction algorithms,” *J. Opt. Soc. Am. A* **35**(2), 275–285 (2018).
- 18 A. Harness, J. Kasdin, S. Shaklan, *et al.*, “Modeling non-scalar diffraction in the Princeton starshade testbed,” *Proc. SPIE* **10698**, 1069865 (2018).
- 19 D. E. Dauger, “Simulation and study of Fresnel diffraction for arbitrary two-dimensional apertures,” *Comput. Phys.* **10**(6), 591–604 (1996).
- 20 J. E. Harvey and J. L. Fordham, “The spot of Arago: new relevance for an old phenomenon,” *Am. J. Phys.* **52**(3), 243–247 (1984).
- 21 A. Dubra and J. A. Ferrari, “Diffracted field by an arbitrary aperture,” *Am. J. Phys.* **67**(1), 87–92 (1999).
- 22 L. Junchang and W. Yanmei, “An indirect algorithm of Fresnel diffraction,” *Optics Comm.* **282**, 455–458 (2009).
- 23 D. Mas, J. Garcia, C. Ferreira, *et al.*, “Fast algorithms for free-space diffraction patterns calculation,” *Optics Comm.* **164**, 233–245 (1999).
- 24 A. F. Oskooi, D. Roundy, M. Ibanescu, *et al.*, “MEEP: A flexible free-software package for electromagnetic simulations by the FDTD method,” *Comput. Phys. Commun.* **181**(3), 687–702 (2010).
- 25 K. Miyamoto and E. Wolf, “Generalization of the Maggi-Rubinowicz theory of the boundary diffraction wave. part ii,” *J. Opt. Soc. Am.* **52**, 626–636 (1962).
- 26 S. R. Hildebrandt, S. B. Shaklan, E. J. Cady, *et al.*, “Starshade Imaging Simulation Toolkit for Exoplanet Reconnaissance (SISTER),” (accessed 9/2/2020). MATLAB software available at <http://sister.caltech.edu/>.
- 27 D. Colton and R. Kress, *Inverse acoustic and electromagnetic scattering theory*, vol. 93 of *Applied Mathematical Sciences*, Springer-Verlag, Berlin, second ed. (1998).
- 28 O. P. Bruno and S. K. Lintner, “A high-order integral solver for scalar problems of diffraction by screens and apertures in three-dimensional space,” *J. Comput. Phys.* **252**, 250–274 (2013).
- 29 A. Dutt and V. Rokhlin, “Fast Fourier transforms for nonequispaced data,” *SIAM J. Sci. Comput.* **14**, 1369–1393 (1993).
- 30 J.-Y. Lee and L. Greengard, “The type 3 nonuniform FFT and its applications,” *J. Comput. Phys.* **206**, 1–5 (2005).
- 31 R. Soummer, L. Pueyo, A. Sivaramakrishnan, *et al.*, “Fast computation of Lyot-style coronagraph propagation,” *Opt. Express* **15**(24), 15935–51 (2007).

- 32 A. H. Barnett, J. F. Magland, and L. af Klinteberg, “A parallel non-uniform fast Fourier transform library based on an “exponential of semicircle” kernel,” *SIAM J. Sci. Comput.* **41**(5), C479–C504 (2019).
- 33 A. H. Barnett, “FRESNAQ: MATLAB/Octave library for fast Fresnel diffraction from apertures and occulters,” (2020). <https://github.com/ahbarnett/fresnaq>.
- 34 L. N. Trefethen, *Approximation Theory and Approximation Practice*, SIAM (2013). <http://chebfun.org/ATAP>.
- 35 B. Vioreanu and V. Rokhlin, “Spectra of multiplication operators as a numerical tool,” *SIAM J. Sci. Comput.* **36**, A267–A288 (2014).
- 36 S. E. Mousavi, H. Xiao, and N. Sukumar, “Generalized Gaussian quadrature rules on arbitrary polygons,” *Int. J. Numer. Methods. Eng.* **82**(1), 99–113 (2009).
- 37 H. Xiao and Z. Gimbutas, “A numerical algorithm for the construction of efficient quadrature rules in two and higher dimensions,” *Comput. Math. with Appl.* **59**(2), 663 – 676 (2010).
- 38 D. Gunderman, K. Weiss, and J. A. Evans, “Spectral mesh-free quadrature for planar regions bounded by rational parametric curves,” (2020). preprint, [arxiv:2005.07780v2](https://arxiv.org/abs/2005.07780v2).
- 39 J. Keiner, S. Kunis, and D. Potts, “Using NFFT 3 — a software library for various nonequispaced fast Fourier transforms,” *ACM Trans. Math. Software* **36**(4) (2009).
- 40 R. Kress, *Linear Integral Equations*, vol. 82 of *Appl. Math. Sci.*, Springer, second ed. (1999).
- 41 N. J. Higham, *Accuracy and Stability of Numerical Algorithms*, SIAM, 2nd ed. (2002).